Numerical Simulation of Diurnal Planetary Boundary Layer Effects and Diurnal Mountain-Wind Effects

Numerisk simulering av effekter från ett diurnalt atmosfäriskt gränsskikt och ett diurnalt bergvindsystem

Robin Isaksson

UPPSALA
UNIVERSITET

DEPARTMENT OF
EARTH SCIENCES

INSTITUTIONEN FÖR
GEOVETENSKAPER

Numerical Simulation of Diurnal Planetary Boundary Layer Effects and Diurnal Mountain-Wind Effects

Numerisk simulering av effekter från ett diurnalt atmosfäriskt gränsskikt och ett diurnalt bergvindsystem

Robin Isaksson

Sammanfattning

Numerisk simulering av effekter från ett diurnalt atmosfäriskt gränsskikt och ett diurnalt bergvindsystem
Robin Isaksson

Prognosmodellen WRF (Weather Research and Forecasting Model) användes för att undersöka hur väl den kunde representera ett område inom ett komplext vindsystem och även hur modellen påverkas av olika val vad gäller drivningsdata och fysikscheman. Det som utgör det komplexa vindsystemet är dygnsvarierande effekter från det atmosfäriska gränsskiktet och dygnsvarierande mesoskaliga effekter från den närliggande bergskedjan Pyrenéerna. Totalt genomfördes sex olika simuleringar. Prognosmodellen kunde representera området men med förbättringsbara resultat eftersom det fanns fel i vindhastighet och vindriktning relaterande till det atmosfäriska gränsskiktet. Modellen var speciellt utmanad i förutsägandet av vindhastighet och vindriktning i ett lager några hundra meter ovanför det atmosfäriska gränsskiktet. En tolkning baserad på atmosfärisk gränsskiktshöjd är dock svår eftersom det fanns flera definitioner var toppen på det atmosfäriska gränsskiktet låg.

Val om prognosmodellens fysikscheman och drivningsdata orsakade en skillnad i resultat sinsemellan. Dessa val bör därför noggrannt uppmärksammas för simuleringar under liknande förutsättningar.

Abstract

Numerical Simulation of Diurnal Planetary Boundary Layer Effects and Diurnal Mountain-Wind Effects
Robin Isaksson

The Weather Research and Forecasting Model was used to study its accuracy and representation in modelling a study area within a complex wind system as well as the effects on the model when using different input data and physics schemes. The complex wind system consists of diurnal mesoscale effects from the nearby Pyrenees mountain range and diurnal effects from the planetary boundary layer. A total of six different simulations were performed. The model was able to represent the study area but the results could be improved as there were inaccuracies in wind speed and wind direction associated with the planetary boundary layer. The model was especially challenged at predicting the wind speed and wind direction in the layer from the top of the planetary boundary layer to few hundred meters above it. The comparisons based on planetary boundary layer height is however complicated by the fact that there are different definitions in effect.

The choice of model physics schemes and input data led to some differences in the results and warrants consideration when conducting similar simulations.

Table of Contents

1 Introduction

The atmospheric boundary layer is the lowest portion of the atmosphere. It has the characteristic of having a quick response to change in surface radiation. The most prominent of such change in surface radiation is the diurnal cycle. Minimum surface radiation occurs during the night with stable conditions in the boundary layer with low amounts of turbulence. As the day progresses the boundary layer react to the increase in solar heating with thermals rising upwards and an increased amount of turbulence. This variation in solar heating has an effect on the wind pattern as it is affected by the turbulence.

The most general description of large scale atmospheric flow is the synoptic atmospheric circulation. Mesoscale effects however influence this flow on a smaller scale where there is influence from the topography. One such influence which is investigated in this project is the diurnal mountain wind system which is characterized by the reversal of wind direction twice per day under fair day conditions (Zardi and Whiteman 2013). Horizontal temperature differences is the mechanism for this departure from the synoptic flow. These temperature differences occur from heating and cooling effects from the diurnal cycle.

The boundary layer together with the mountain wind system gives rise to a more complicated system in regard to the temporal evolution of the wind-profile. The Boundary Layer Late Afternoon and Sunset Turbulence (BLLAST) field campaign (BLLAST 2011a) collected observations in such a system at the northern base of the Pyrenees and can provide resources for evaluating simulations done for the area.

The project purpose is to investigate how well the WRF model can simulate a fair weather situation with effects from both the atmospheric boundary layer and from the diurnal mountain wind system which is present on the northern base of the Pyrenees. This is accomplished by comparing the WRF-output from a reference simulation with BLLAST observations from in situ windprofilers and radiosondes. Another objective is to study the simulation sensitivity to input data and how the difference in the choice of physics scheme affect the results. This is achieved by doing several simulations with minimal differences from the reference simulations such that they can be compared. These objectives are useful to achieve as increased knowledge of the effects topography and the boundary layer has on the wind profile is important for understanding the impact complex terrain like the Pyrenees has on the weather and climate. Knowledge of how to simulate such a complex wind system is also important in areas such as the evaluation of wind energy sites.

2 Background and Theory

2.1 Study Area

The study area encompasses a large portion of France and Spain (from $4°W$ to $6°E$ and $39°N$ to $47°N$). Most notable in the study area is the Pyrenees mountain range. The Pyrenees is located in the midlatitudes extending along the border between France and Spain with the Meditteranean sea to the east and the Atlantic ocean to the west.

On a synoptic scale the region has an oceanic influence with prevalent westerlies which weaken over the continent towards the east (Quéno et al. 2016). The mountain range has complex topography with 129 documented peaks above 3000 m.a.s.l. with the highest being 3404 m.a.s.l. (Reynolds 1995).

An important location for this study is where the `BLLAST` field campaign was conducted at, a site called *Plateau de Lannemezan*. It is a plateau on the northern side of the Pyrenees mountain range nearby its foothills. The plateau spans about 200 km^2. Plateau de Lannemezan is located at nearly equal distance from the Mediterranean sea and the Atlantic ocean with this distance being roughly 200 km. Further a south-north oriented valley named *Vallée d'Aure* has its exit directly south of the plateau (BLLAST 2011b).

The weather during the study period (June 20 2011 to June 21 2011) is a high pressure system centered in southern France, north of the Pyrenees. This high pressure system is moving westward during the study period.

2.2 Planetary Boundary Layer

The planetary boundary layer is the lowermost portion of the atmosphere which interacts with the terrain by the mechanics of solar radiation. Solar irradiance warm the ground which in turn heats adjacent air masses causing them to rise. This rising air is a flux of buoyancy and forms a convective boundary layer. The air inside the boundary layer is turbulent and well mixed. The boundary layer deepens as the solar irradiance peaks at midday and reaches its maximum for a few hours until it starts to decrease in depth towards the afternoon. During nighttime the boundary layer is shallow as the terrain instead has a cooling effect from emitted thermal radiation.

The planetary boundary layer is important in the discussion of wind speed and wind direction. Wind inside the planetary boundary layer experience drag effects from the surface, which effectively means that the wind will turn against the isobars (lines of constant pressure) i.e. towards the region with lower pressure.

Some effects the planetary boundary layer has on winds can be explained from Newton's second law and the governing forces in the movement of air. Consider a parcel of air with mass m, subject to acceleration a. The four main forces in the meteorological context are the pressure gradient force (`PGF`), the Coriolis force, the gravitational force and the drag force induced from surface friction. For these forces Newton's second law yields:

$$m\mathbf{a} = \mathbf{F}_{\text{PGF}} + \mathbf{F}_{\text{Coriolis}} + \mathbf{F}_{\text{friction}} + \mathbf{F}_{\text{gravity}} \tag{1}$$

In this discussion it is only necessary to note which forces are velocity-dependent and which are not. The pressure gradient- and gravitational force have no velocity components whereas the Coriolis- and frictional force do.

Winds above the planetary boundary layer are approximated to experience no friction. Considering horizontal motion, the balance between the pressure gradient force and the Coriolis force is what is called the geostrophic wind. As a parcel of air starts to accelerate and move against the pressure gradient the Coriolis force acts orthogonally to the direction of the parcel (accelerating the parcel to the right on the north-

ern hemisphere and to the left on the southern hemisphere). The Coriolis force is linearly velocity-dependent and cause the parcel to turn outward from the pressure gradient. This turning motion will with enough time (and with close to stationary conditions) align the wind to be at a right angle to the horizontal pressure gradient where the force from the pressure gradient is completely counteracted by the Coriolis force (see figure 1).

$$\mathbf{F}_{\text{PGF}} + \mathbf{F}_{\text{Coriolis}} = 0 \tag{2}$$

How does then the planetary boundary layer affect winds? Winds inside the planetary boundary layer are non-geostrophic as they experience a frictional drag force. This drag force acts with opposite direction to the motion of the parcel. As the Coriolis force is velocity dependent this effect reduces its magnitude. The resulting wind is the non-geostrophic wind which does not fully align with the isobars and is shown in figure 2.
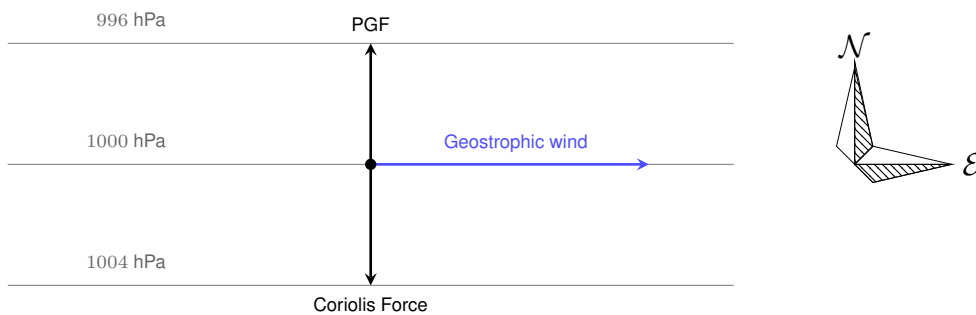
Figure 1. Force diagram with balanced pressure gradient force and Coriolis force in the absence of drag. The resulting wind is the geostrophic wind which has a direction parallel to the isobars. This is an approximation of winds outside the planetary boundary layer.
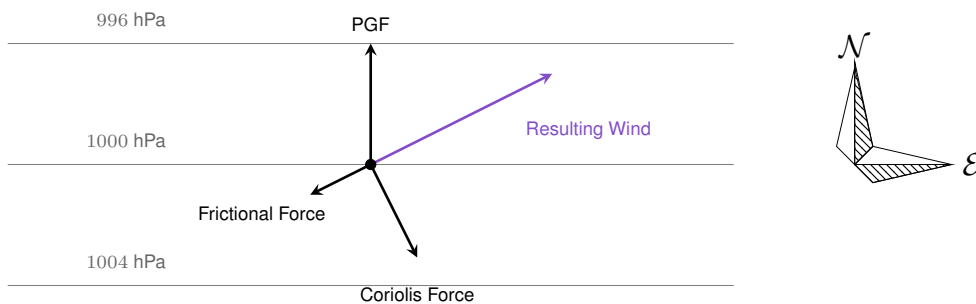
Figure 2. Force diagram with an introduced frictional drag force. The velocity dependent Coriolis force decrease in magnitude while the pressure gradient force's magnitude is unaltered. The resulting wind turns against the pressure gradient. Winds inside the planetary boundary layer experience terrain friction and undergoes this directional change.

2.3   Diurnal Mountain-Wind Systems

The terrain at *Plateau de Lannemezan* is a subset of a *diurnal mountain wind system* which is the *mountain-plain wind system*. Additionally Plateau de Lannemezan is aligned with a valley which is a different subset of the diurnal mountain-wind system called a *valley wind system*. Diurnal mountain wind systems are systems which experience a temporal evolution in wind directions and wind speeds. The wind change direction typically twice per diurnal cycle during fair weather conditions. Similarly to the formation of the planetary boundary layer the diurnal mountain wind systems are thermally driven and hence forms more easily in fair weather conditions. The diurnal mountain-wind systems are closed circulations with aloft return flows. The general flow of a mountain wind system can be seen in figure 3 with the Appalachian mountains as an example.

To understand the mountain wind systems it is beneficial to understand the *slope-wind system* which is a simpler system but highly related to the mountain wind systems. The slope-wind system is a thermally driven system. The driving action of the slope-wind system is solar irradiance from the diurnal cycle. Solar irradiance causes the formation of a boundary layer with heated air close to the surface. This causes the air inside the boundary layer to thermodynamically expand and to rise upwards along the slope. This rising movement of air is called an upslope wind. When the solar irradiance has subsided (evening, sunset) the terrain is radiatively cooled causing the air near the mountain terrain to cool and contract with increased rate. The air close to the terrain is then denser and sinks compared to the surrounding atmosphere, leading to downslope winds.

According to Ahrens and Samson (2009) Plateau de Lannemezan might experience weak upslope winds since they are weaker on the north-facing slopes. The upslope winds are strongest on the south-facing slopes.

The Valley-Wind system is a combination of the slope-wind system with another thermal effect. The valley winds blow along the valley, upwards the valley during the day and downwards during the night. Some of this movement of air is slope-winds. The other cause of this effect is a temperature gradient along the valley which results in a pressure gradient force which causes the wind to move from the warmer area to the colder area. Valley winds do therefore not necessarily require a slope and has a distinction from the more general slope-wind system. The valley cross-section is very conducive to slope flows and thus the valley-sides experience upslope winds during the day and downslope winds during the night (further illustration in figure 4). These valley-side winds can also lead to channeling effects in the main valley flow direction.

The Mountain-plain wind system is a system with large scale terrain being a mountain in adjacency to a plain. There is a difference in terrain heating- and cooling on the plain and the slopes of the mountain. Similarly to the valley-wind system this moves air by the pressure gradient force and the movement of air is subsequently amplified by the slope-wind system as it reaches the mountain massif.
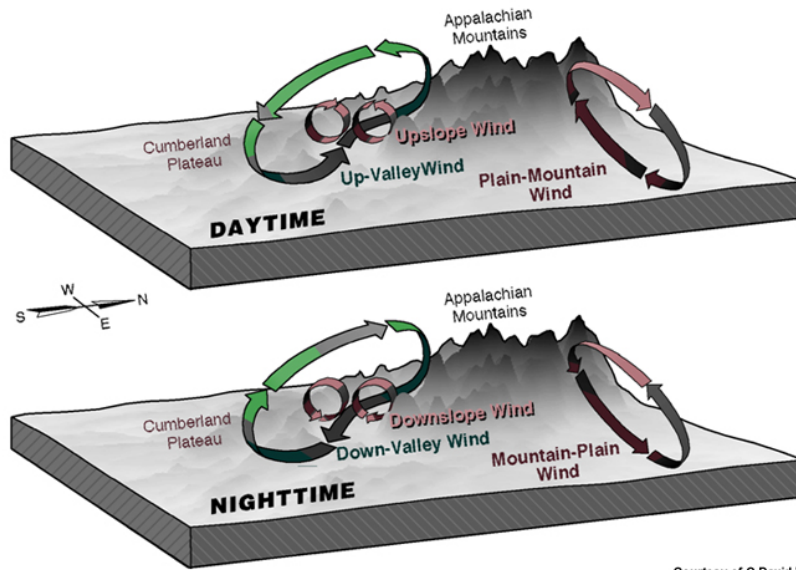
Figure 3. Daytime and nighttime depiction of diurnal mountain wind systems in the Appalachian Mountains (Whiteman 2014). The general circulation and aloft return flows are seen for both the valley wind system and the mountain-plain wind system.

Daytime   Nighttime
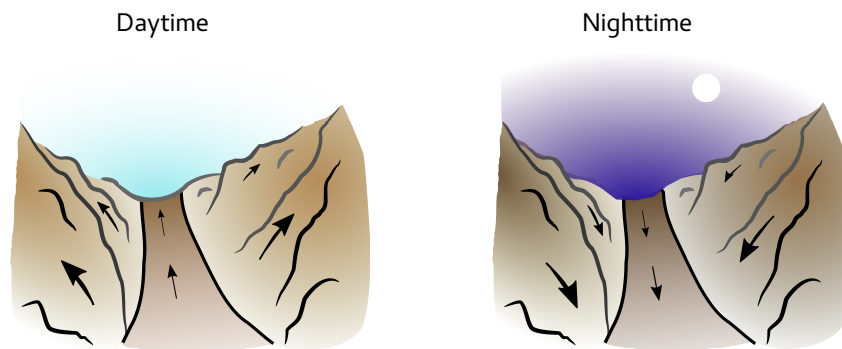
Figure 4. Valleys experiences both up- and down valley flow as well as up- and down slope flow along the valley sides dependent on the time of day.

2.4   Weather Research and Forecasting Model (WRF)

WRF is a numerical weather prediction software and a model which to simulate the atmosphere. It is a open-source community driven project with applications in both forecasting and research (Skamarock et al. 2008).

The version of WRF used in this project can be generalized to consist of two parts. The WRF Preproccessing System WPS and the Advanced Research WRF (ARW) which contain the ARW dynamic solver and physics packages.

WPS is a system of programs which are used to transform and format model input data to ARW such that it can be used in the model. This input data consists of static terrestrial data (e.g. terrain height) and non-static meteorological data.

ARW is the WRF atmospherical model which does the numerical weather prediction. ARW contain different physics packages such that the atmosphere can be modelled by using different physics schemes. Different physics schemes can be used for *microphysics, cumulus parameterizations, surface physics, planetary boundary layer physics* and *atmospheric radiation physics*.

2.4.1 WRF Coordinate System

WRF is a cell-based model which subdivides the model domain into a finite number of three-dimensional cells. The horizontal resolution describe the horizontal extent of each cell. The cell's vertical resolution is however variable as the vertical extent of the cell adapts to the terrain. The terrain-following vertical coordinate scheme employed by WRF is called an *eta* (η) scheme and is based on hydrostatic pressure. The relation between hydrostatic pressure p and η-levels involves the hydrostatic pressure at the *top of the domain* p_{top} and a standard *reference pressure* (chosen to be the standard atmospheric pressure at mean sea level) $p_{\text{reference}}$ and is formulated as:

$$\eta = \frac{p - p_{\text{top}}}{p_{\text{reference}} - p_{\text{top}}} \tag{3}$$

(The COMET® Program 2009). The η-coordinates are defined by the user and normally goes between a value of 0 at the top of the domain and 1 at the surface level. Figure 5 below show a typical behavior for this dynamic coordinate.
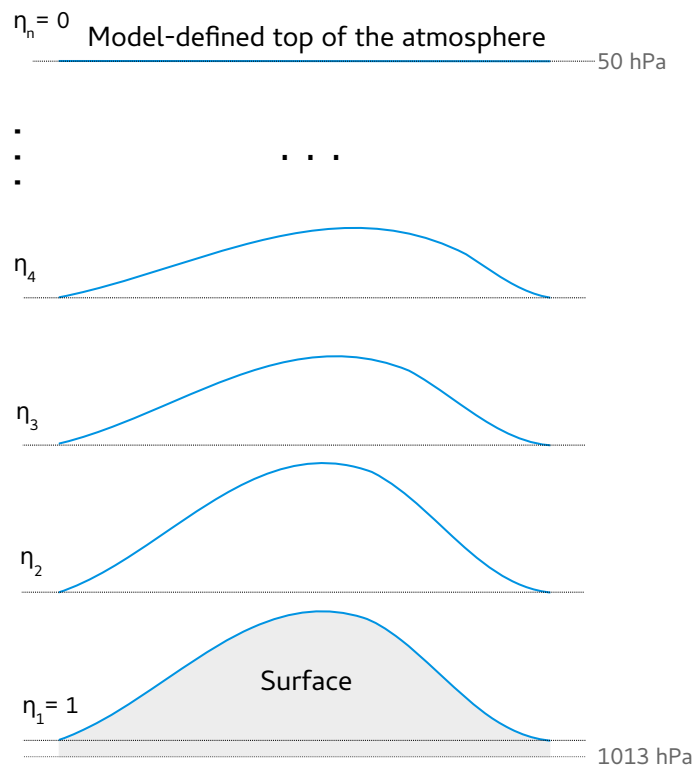
Figure 5. The terrain-following nature of the η-coordinate. The top of the atmosphere in this example is defined at 50 hPa.

WRF is as mentioned cell-based, however the variables are *staggered* and follow an *Arakawa C-grid* which I will explain further shortly. It is important to understand in which way the variables are ordered in the grid. The most simple Arakawa grid is the Arakawa A-grid where all variables are evaluated at the same point in each grid (e.g. the center of each grid) and might be what one intuitively presumes the model to use. The Arakawa A-grid is an *unstaggered* grid model as there are no different point

in the same grid which different variables are defined at. The Arakawa C-grid which WRF uses is staggered both horizontally and vertically and can be seen in figure 6. Thermodynamic variables are defined at the center of each cell (e.g. variables relating to temperature or moisture). Wind components are defined at the center of the cell faces; the east-aligned wind component u is defined at the east cell face and the north-aligned wind component v is defined at the north cell face. The vertical staggering is the same where the upwards-wind component w is defined at the center of the cell's top face. WRF implements the Arakawa C-grid as it has an effective higher resolution than an unstaggered grid (Collins et al. 2013).
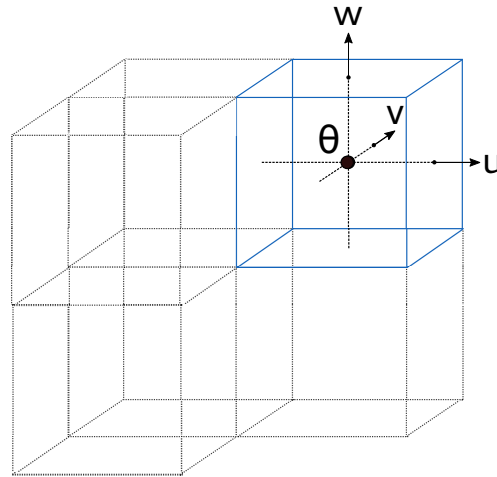
Figure 6. The WRF Arakawa C-grid with staggering both horizontally and vertically. Wind-components are defined at the center of the cell faces (u, v, w) while thermodynamic components are defined at the cell center (θ).

2.4.2 Domain Nesting

Nesting is a useful concept in regards to large scale simulations. Nesting is the act of defining additional domains inside large-scale domain (called the *parent domain*). The smaller domains which exist within the parent domain bring a lot of advantages. In WRF they are allowed to have different settings than the parent domain. This for example allows inner domains to have a higher resolution than the parent domain. This is useful for large-scale simulations where there exists areas of special interest. High resolution may then only be applied where it is necessary and effectivizes the simulation. The inner domains can also have different physics settings to customize the simulation (for example in WRF there are physics settings which are not suitable for low resolution domains but might be for higher resolution domains).

In regard to nesting in WRF there are two different disciplines which relate to how the parent- and inner domains interact. The parent domain always provide boundary conditions to the inner domains. If this is the only mechanism of interaction between the domains it is a one-way trade of information and is called *1-way nesting*. The inner-domains can feedback information to the parent domain, which is then replacing the parent cell's simulated variables at parent cells which lie within the inner domains. This is a two-way trade of information and is called *2-way nesting* (Skamarock et al. 2008). A visualization of 2-way nesting can be seen in figure 7.

Figure 7. 2-way nesting between a parent domain with coarse resolution and a sub-domain with higher resolution. The parent domain will provide boundary conditions to the sub-domain while the sub-domain will provide solutions to the parent domain.
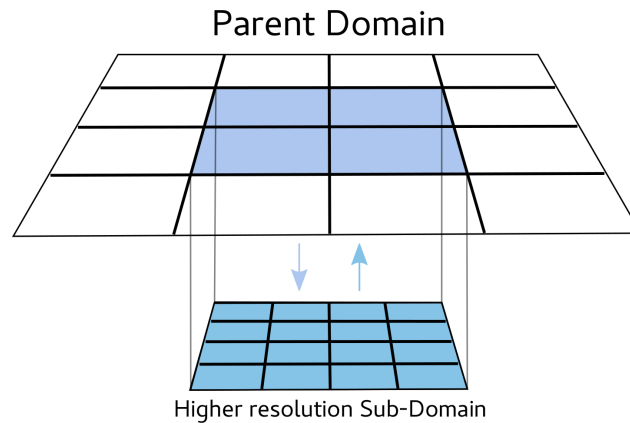
2.4.3 WRF Input Data

As discussed WRF requires non-static meteorological data to perform real (non-ideal) numerical weather prediction and atmospheric modelling. WRF require this meteorological data to initialize each of the model cell as well as it is required to provide boundary conditions.

This input data can be obtained from different sources. As different sources of meteorological data will differ in values this will drive the model to different results. It is because of this reason interesting to use two different sets of input data to see how pronounced the effect from the differences in driving data is in the results.

2.4.4 Planetary Boundary Layer Parameterization Schemes

The planetary boundary layer schemes are used to parameterize unresolved fluxes such as heat, momentum and moisture due to turbulent transport in each atmospheric column (and not just inside the planetary boundary layer as the name might suggest). The planetary boundary layer scheme interface with the surface layer and surface schemes as they provide surface fluxes to the planetary boundary layer scheme (Skamarock et al. 2008).

The planetary boundary layer parameterization can be done using different approaches. These differing approaches arise from the *turbulence closure problem* which is the unresolved nature of corrective terms when modelling turbulent transport, which mean some variables must be parameterized. These approaches to parameterize the unresolved variables are categorized as having different *orders* and *locality*. The order of closure relate to which level of correctional terms that are used, more variables are parameterized with higher order of closures. The locality describes the approaches for the cells' boundary layer parameterizations. A *local closure* model uses only values from vertical grid points in a close vicinity to parameterize the unresolved variables whereas a *non-local closure* model might use any number of vertical grid points to parameterize the unresolved variables (Stensrud 2007 Hu, Nielsen-Gammon, and Zhang 2010). As this project focus on the WRF model's representation of plan-

etary boundary layer effects these different approaches are expected to impact the results, especially when comparing a local and non-local scheme.

2.4.5 Cumulus Parameterization Schemes

The *cumulus parameterization* describe sub-grid-scale effects from convective and shallow clouds by parameterizing vertical up- and down-drafts. Cumulus parameterization is designed for low-resolution grid sizes and as such should preferably only be used on coarser model grids. The cumulus parameterization are grid-column specific and act on the single column by introducing vertical heating and moistening profiles (Skamarock et al. 2008).

3 Method

WRF version 3.7.1 was used to simulate the domain area for a 30 hour period. The same domain and time period was used for all simulations. The time period is June 20 2011 00:00 UTC to June 21 2011 06:00 UTC. This time period with focus on June 20 was chosen as it was a day with intensive observations in the BLLAST field campaign and was a sunny day with little clouds and no rain (BLLAST 2015). BLLAST researchers performed atmospherical observations with radiosondes throughout the day as well as observations with wind profilers.

WRF was configured with a timestep of 30 seconds. The model domain (see figure 8) was nested with a coarse parent domain with 9 km horizontal resolution and a nested sub-domain with horizontal resolution of 3 km which is a 3:1 nesting ratio. The sub-domain was 2-way nested to the parent domain for all simulations. Variables are outputted every 15 minutes which means that the output data has a temporal resolution of 15 minutes.

Each simulation was set up with the same set of 50 η-levels with top of the atmosphere chosen to be 50 hPa. They were chosen with high density of levels near the value 1 with the η-level density decreasing towards the final value of 0. This means that the model collects more variables near the surface ($\eta = 1$ at the surface) which is the area of focus of this project. This corresponds to 29 vertical levels below 1000 m above the surface. The complete set of η-levels can be found in table 1. η-levels as well as general physics settings are mostly the same as used in Angevine et al. (2014) which conducted a WRF simulation in the same area in conjunction with the BLLAST field campaign and as such provides a good reference for WRF parameters.

A full configuration (`namelist.input`) of the reference run is provided in Appendix B.
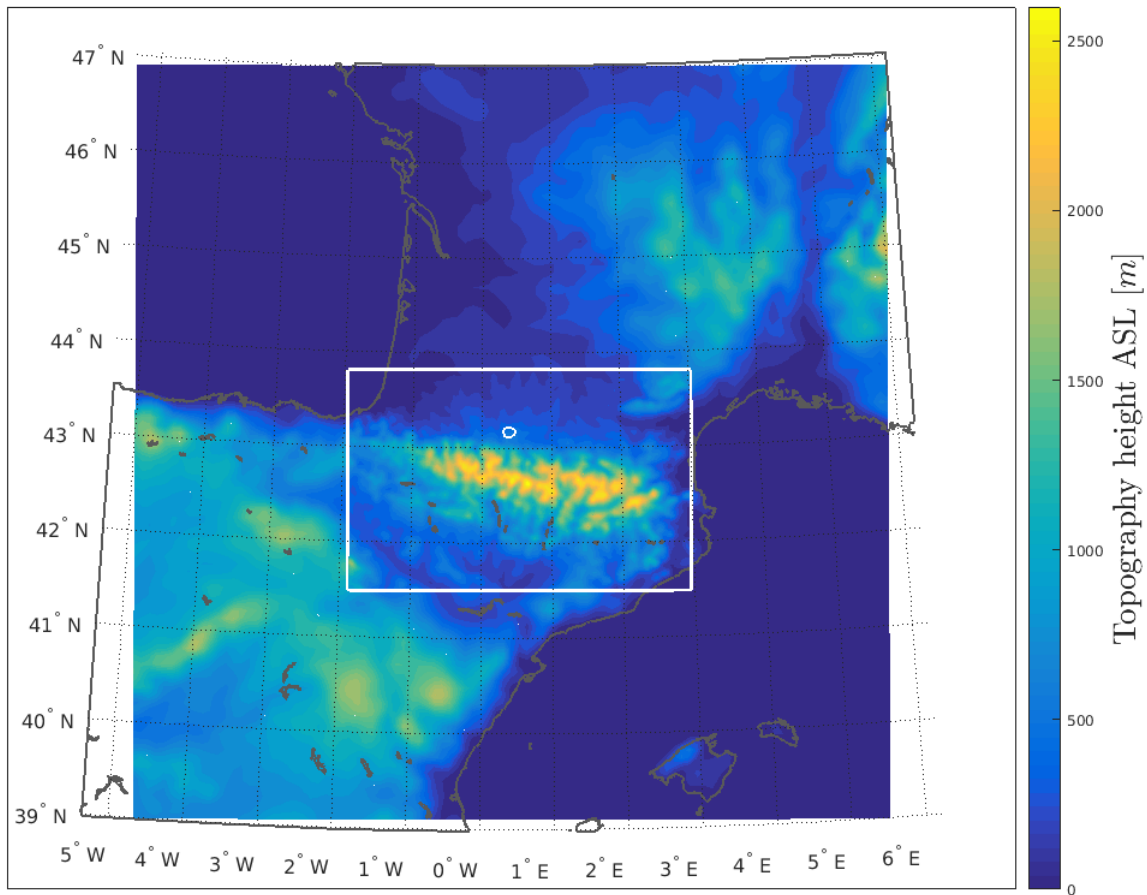
Figure 8. The WRF domain with color coded topography. The white border indicates where the sub-domain is located i.e. the finer resolution domain. The white marker indicates the location of *Plateau de Lannemezan* where in situ observations have been made in the BLLAST field campaign.

Table 1. The set of η-levels that were used for each WRF simulation in this project. The density of vertical levels is highest near the surface.

$$
\begin{aligned}
\eta = \quad & 1.000, \quad 0.999, \quad 0.998, \quad 0.997, \quad 0.996, \\
& 0.995, \quad 0.994, \quad 0.993, \quad 0.992, \quad 0.991, \\
& 0.990, \quad 0.988, \quad 0.986, \quad 0.984, \quad 0.982, \\
& 0.980, \quad 0.978, \quad 0.976, \quad 0.974, \quad 0.972, \\
& 0.970, \quad 0.960, \quad 0.950, \quad 0.940, \quad 0.930, \\
& 0.920, \quad 0.910, \quad 0.900, \quad 0.890, \quad 0.880, \\
& 0.870, \quad 0.860, \quad 0.850, \quad 0.840, \quad 0.830, \\
& 0.820, \quad 0.810, \quad 0.800, \quad 0.750, \quad 0.700, \\
& 0.650, \quad 0.600, \quad 0.550, \quad 0.500, \quad 0.450, \\
& 0.400, \quad 0.300, \quad 0.200, \quad 0.100, \quad 0.000
\end{aligned}
$$

3.1 WRF Simulations

A reference simulation was done using ERA-interim input data with MYJ PBL-scheme and KF cumulus parameterization. Five additional simulations were done to study the effects of changes in input data and physics schemes. The simulations are summarized in table 2.

Table 2. The WRF simulations and their different settings are summarized. Note that the YSU PBL scheme requires a different surface layer option which is not shown in this table. The cumulus scheme is only applied to the coarse, outer domain.

Simulation Number	Input data	PBL scheme	Cumulus scheme
1	ERA	MYJ	KF
2	FNL	MYJ	KF
3	ERA	MYNN 2.5	KF
4	ERA	YSU	KF
5	ERA	MYJ	BMJ
6	ERA	MYJ	none

3.2 Input Data

Two different data sets were used, the National Centers for Environmental Prediction FNL (Final) Operational Global Analysis data set (denoted in short by FNL) which is provided by NCEP's Global Forecast System (UCAR 2016a) and the European Centre for Medium-Range Weather Forecasts ERA-Interim Re-analysis data set denoted by ERA (ECMWF 2016).

3.3 Physics Schemes

Three different planetary boundary layer parameterization schemes have been used in the project WRF simulations: *Mellor-Yamada-Janjic* (MYJ), *Yonsei University* (YSU) and *Mellor–Yamada–Nakanishi–Niino* (MYNN). The MYJ planetary boundary layer scheme is a TKE-based local closure model of order 1.5 where TKE abbreviates turbulence kinetic energy. The YSU planetary boundary layer scheme is non-TKE non-local closure scheme of first order. The MYNN 2.5 planetary boundary layer scheme used is a TKE-based local closure scheme of order 2.5. It is important to note that the MYNN scheme requires certain model surface layer schemes. More information about these schemes can be acquired from Skamarock et al. (2008).

Two different cumulus parameterization schemes were used. Only the coarse domain used any cumulus parameterization as the nested sub-domain had resolution high enough to adequately resolve such convective events. The *Betts-Miller-Janjic* (BMJ) cumulus parameterization scheme was one of the two cumulus schemes used. BMJ is based on the Betts-Miller cumulus parameterization scheme. The other cumulus scheme is the *modified Kain-Fritsch* scheme KF. More information about these schemes can be found in Skamarock et al. (ibid.).

3.4 Data Analysis

The WRF simulation outputs NetCDF datafiles containing the simulation variables, separating each model-domain in files. With the WRF output data I used the NCAR Command Language (NCL) (more information about NCL at UCAR (2016b)) to format the data and to perform interpolations from the model's vertical η-levels to linearly spaced vertical levels in height above ground. With the formatted and interpolated data I used MATLAB to read, filter, compute and to compare the data to wind profiler data and radiosonde data to finally visualize the results in figures and tables.

To compare BLLAST radiosonde- and wind-profiler data I bilinearly interpolated the observational data to align with the interpolated WRF coordinates. The radiosondes had an abundance of vertical measurements and were thus downsampled by taking the mean value of all measurements down- and up 25 m in 50 m steps, producing the WRF linear vertical coordinates. The wind profiler data was bilinearly interpolated more simply by choosing the wind-profiler time-coordinates that were closest to WRF data and then linearly interpolating the required data, such as wind components.

The wind profiler observations provide an estimate of PBL depth based on *air refractive index structure coefficient* (Couvreux et al. 2016). This estimate was used to define three different PBL-layers, the bottom half of the PBL, the upper half of the PBL and a part 500 m above the PBL. These regions were used to isolate datasets and perform comparisons in the context of the PBL (figure 18 can serve as an illustration of the PBL dependent layers of interest). The analysis is divided in time as well. Three different 6 hour time periods are used. From 06:00 UTC June 20 to 12:00 UTC June 20, from 12:00 UTC June 20 to 18:00 UTC June 20 and from 18:00 UTC June 20 to 00:00 UTC June 21. The periods correspond roughly to 1, unstable conditions with growing amounts of turbulence in the planetary boundary layer; 2, unstable conditions with decaying amounts of turbulence and 3, stable night-time conditions.

Radiosonde data was similarly isolated with respect to the planetary boundary layer, this time the WRF estimate of the PBL depth was used to filter the data into data inside, and outside up to 500 m above the PBL.

The values falling inside these periods and layers were condensed to *mean values*. Any comparison between values used the *mean absolute errors* $\varepsilon_{\mathrm{abs}}$. The mean absolute error is here defined as

$$\varepsilon_{\mathrm{abs}} = \frac{\sum_i^n |a_i - b_i|}{n} \tag{4}$$

where a and b are the two variables compared and n is the number of elements associated with each variable. I will also denote this quantity as the *mean absolute difference* to distinguish a comparison of model values to observed values (*errors*) and model values with other model values (*differences*).

4 Results

Results from the six WRF simulations are presented here and subdivided into sections. The reference simulation will have more results presented as it is used to study the WRF representation of the study area. These results are beneficial in presenting

an overview of the situation. Results are more sparsely presented for following WRF simulations where tables sufficiently describe necessary comparisons.

4.1 Reference Simulation

4.1.1 Wind Fields

An instantaneous top-down view of the near-surface horizontal wind field is presented in figure 9 and 10 for the time 12:00 UTC and 00:00 UTC respectively. The daytime upslope mountain flow characteristics are visible along the mountain faces and valleys as is the nighttime downslope flow characteristics. The difference between daytime and nighttime is readily observed in the two figures, especially along the northern mountain faces.
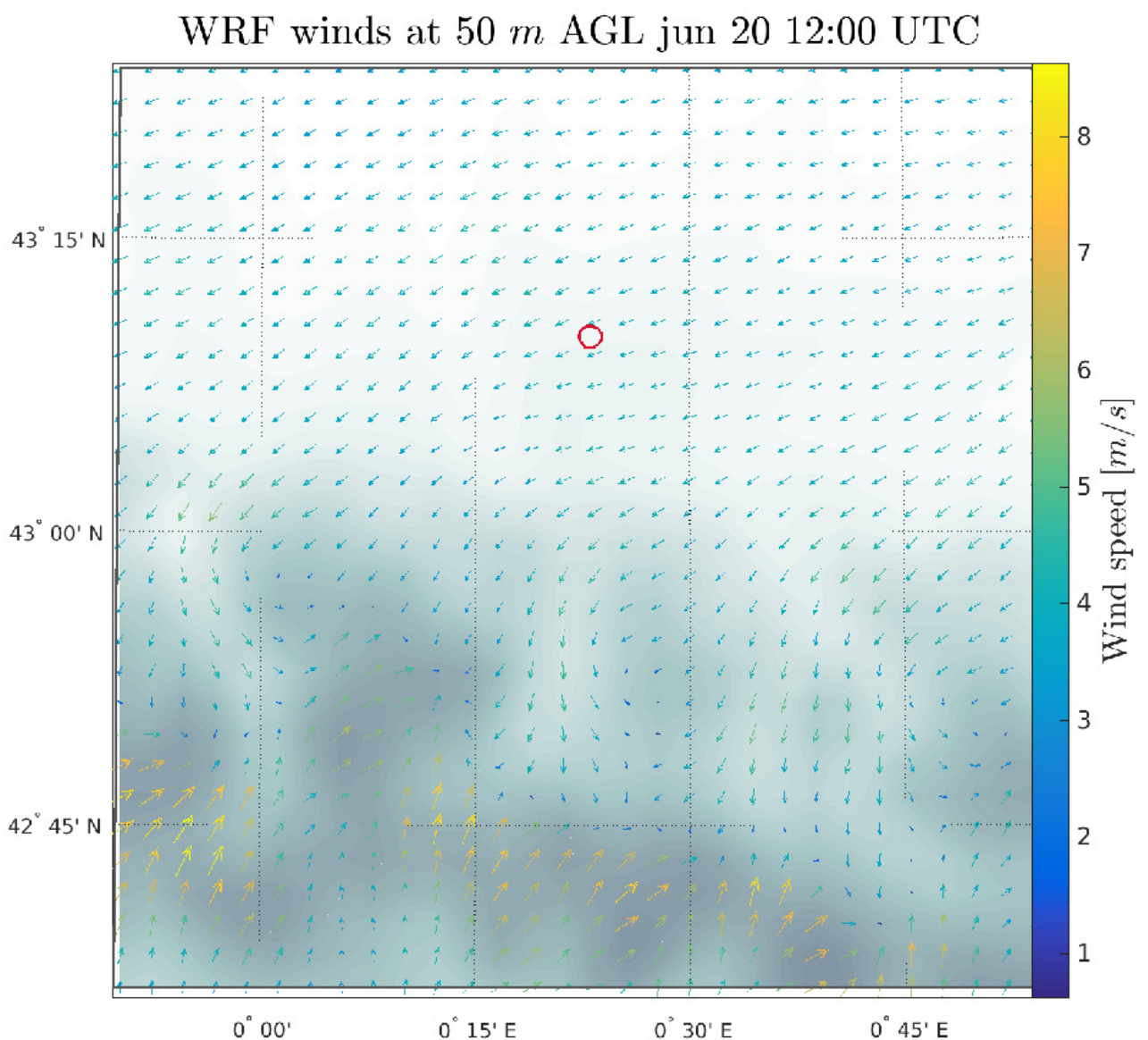
Figure 9. Horizontal wind field at near-surface levels during daytime (12:00 UTC). The red marker indicates the position of *Plateau de Lannemezan*. The shaded background indicates topography with darker regions being higher-leveled surfaces.
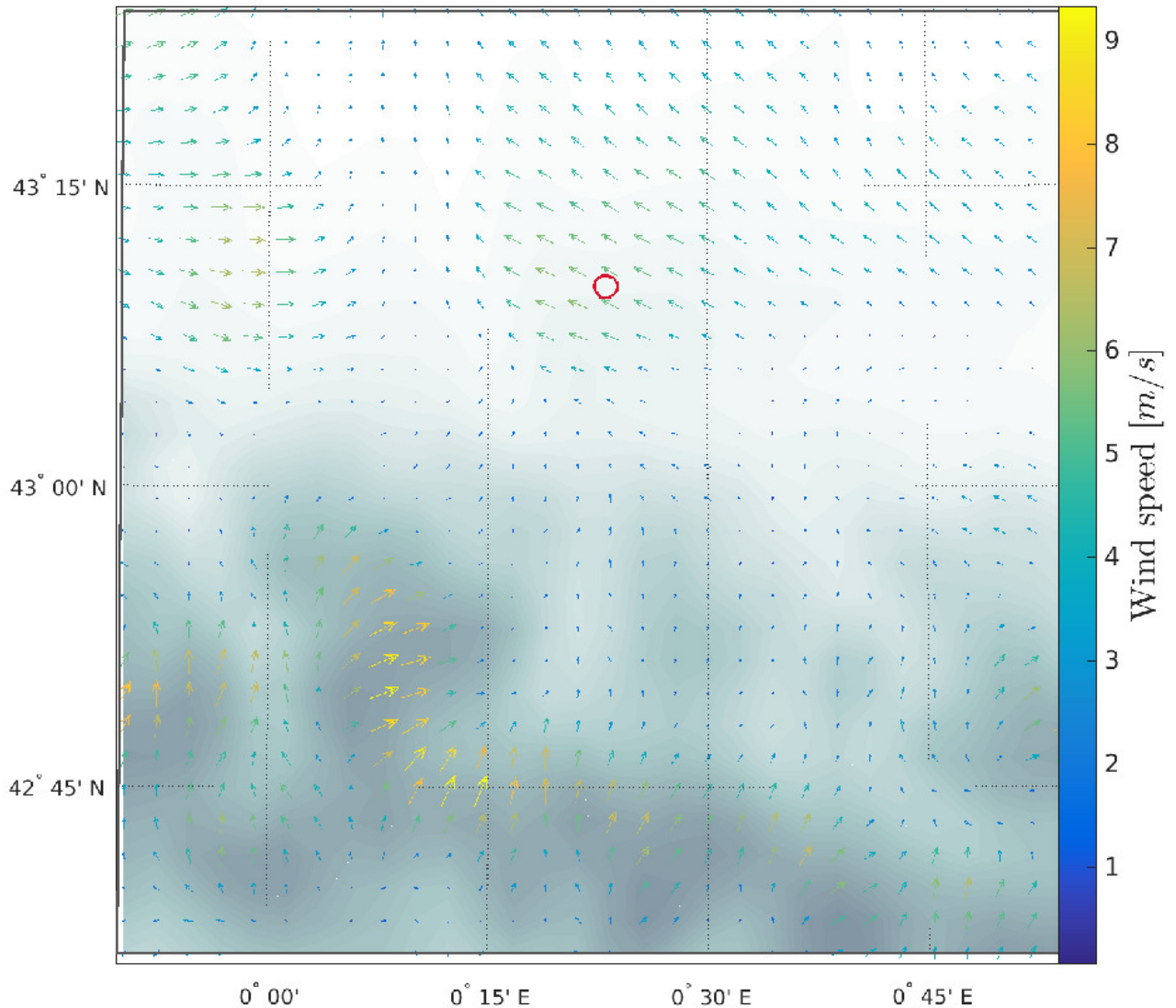
Figure 10. Horizontal wind field at near-surface levels during nighttime (00:00 UTC). The red marker indicates the position of *Plateau de Lannemezan*. The shaded background indicates topography with darker regions being higher-leveled surfaces.

Figure 11 show a vertical and temporal profile of the horizontal wind. The winds near the surface are easterly at *Plateau de Lannemezan* but the figure show an aloft westerly flow which diminish as the boundary layer forms as the wind turns southward towards the Pyrenees. The figure also seem to indicate that the downslope flows indeed are stronger in comparison to the daytime upslope flow as the surface winds have very weak southward facing components.
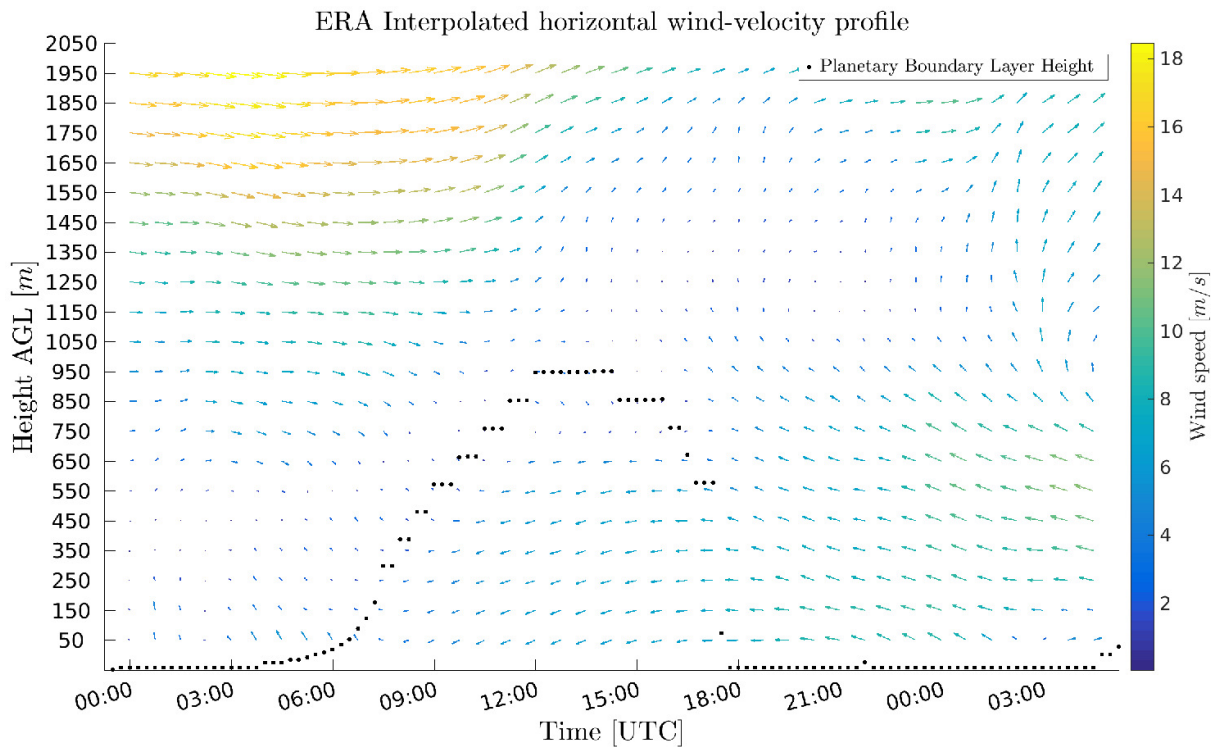
Figure 11. Horizontal wind profile generated by WRF. Values shown are interpolated from WRF η-levels to the linearly spaced horizontal levels shown in the left vertical axis. The WRF generated PBL height is marked with black dots. An arrow pointing upwards means a mean local southerly wind (directed to the north).

The WRF simulated planetary boundary layer height compared to the wind profiler measurements is seen in figure 12. The standard boundary layer height output from WRF is seen as red markers. The definition of boundary layer height used by WRF is similar to the TKE dissipation rate estimate (green markers) rather than the estimation from the air refractive index structure coefficient (black and blue markers). The different definitions of planetary boundary layer height is explained further in Couvreux et al. (2016). Compared to the air refractive index structure coefficient estimate WRF severely overestimated the rate the boundary layer dissipates as the sun starts to set. The maximum boundary layer height was mismatched as well as the time period the boundary layer was formed. Compared to the TKE dissipation rate estimate WRF more accurately follow the trend of the boundary layer formation and dissipation, however overestimating the height. Both boundary layer height estimates from the wind profiler show some activity during the evening which WRF have no representation of.
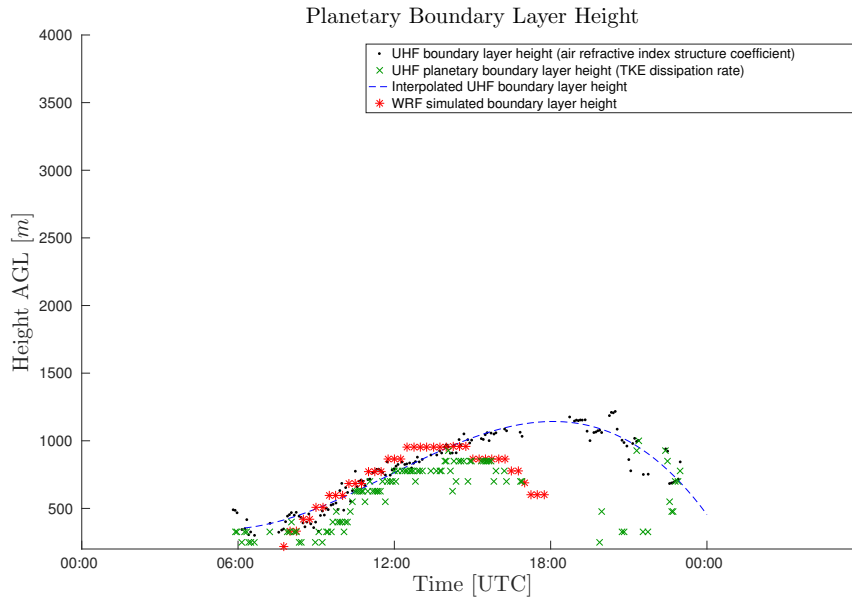
Figure 12. Planetary boundary layer height as measured by a wind profiler and as predicted by the WRF reference simulation.

Figure 13 and 14 show how well the reference WRF simulation were able to simulate the atmosphere at *Plateau de Lannemezan* by comparing the results observed with a wind profiler. In figure 13 it is seen that the WRF simulation underestimates the magnitude of the wind speed a few hundred meters above the boundary layer. WRF generally underestimates wind speed. The wind-direction fields seen in figure 13 are also wrongly predicted by WRF a few hundred meters above the planetary boundary layer. It is however important to note that WRF predicted a low wind speed at these areas which mean that the predicted wind-direction has less importance. The high level fields are however quite accurate. The wind-direction calculations done in these figures weights the direction with the directional wind components.
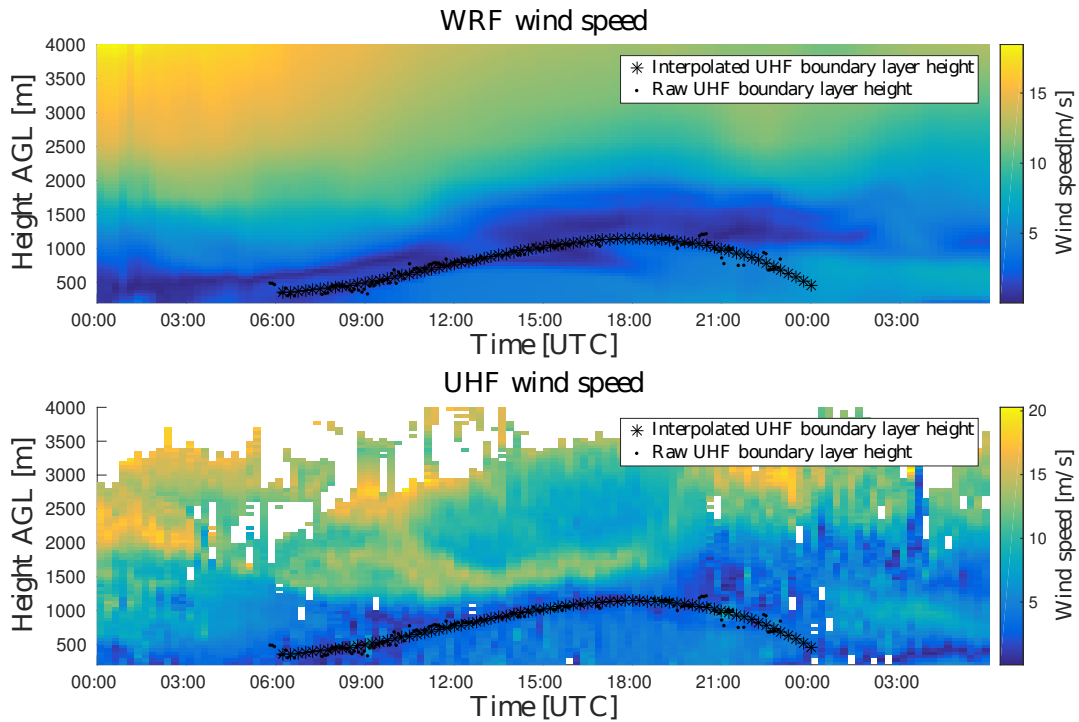
Figure 13. Temporal wind speed profile as predicted by WRF (top) and as observed by a UHF-wind profiler (bottom). The planetary boundary layer is shown with markers. The white areas are missing wind-profiler observations.
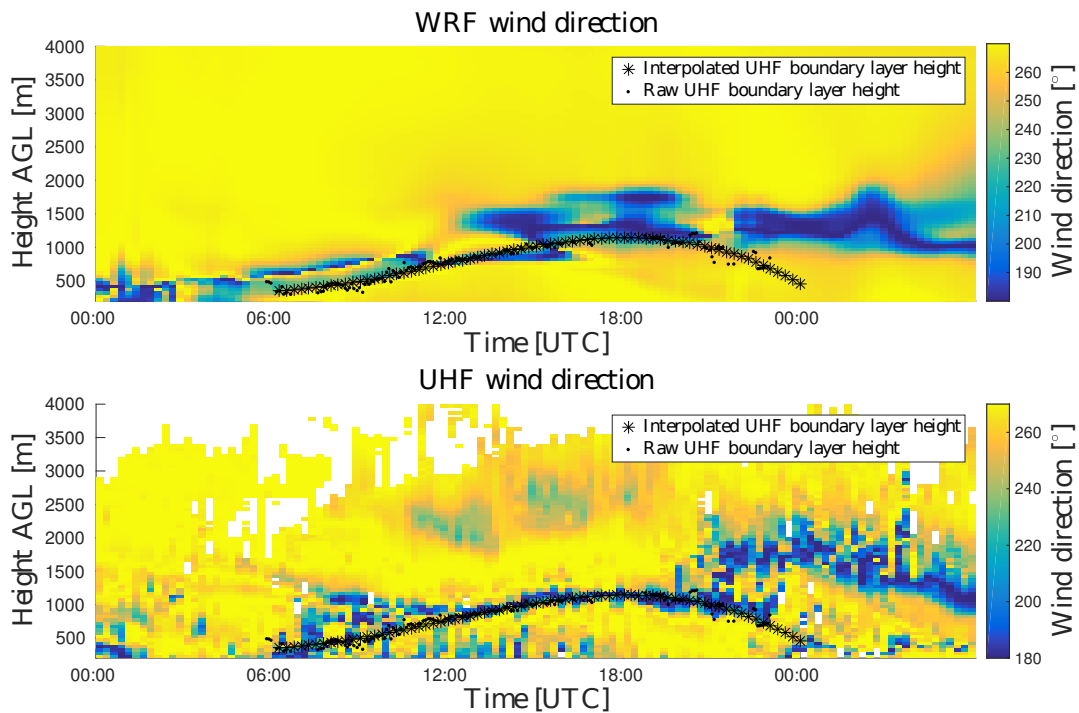
Figure 14. Temporal wind direction profile as predicted by WRF (top) and as observed by a UHF-wind profiler (bottom). The planetary boundary layer is shown with markers. The white areas are missing wind-profiler observations.

4.1.2 Comparison with Radiosondes

Results and comparisons relating to observations made with radiosondes at *Plateau de Lannemezan* are presented here. These comparisons are based on potential temperature, wind speed and wind direction.

Vertical potential temperature profiles are seen for five periods in figure 15. The WRF reference simulation potential temperature is presented together with potential temperature observations from radiosondes. WRF generally underestimates the potential temperature where around 1000 m to 2000 m is a problematic area with larger differences. The differences diminish at increasing heights.
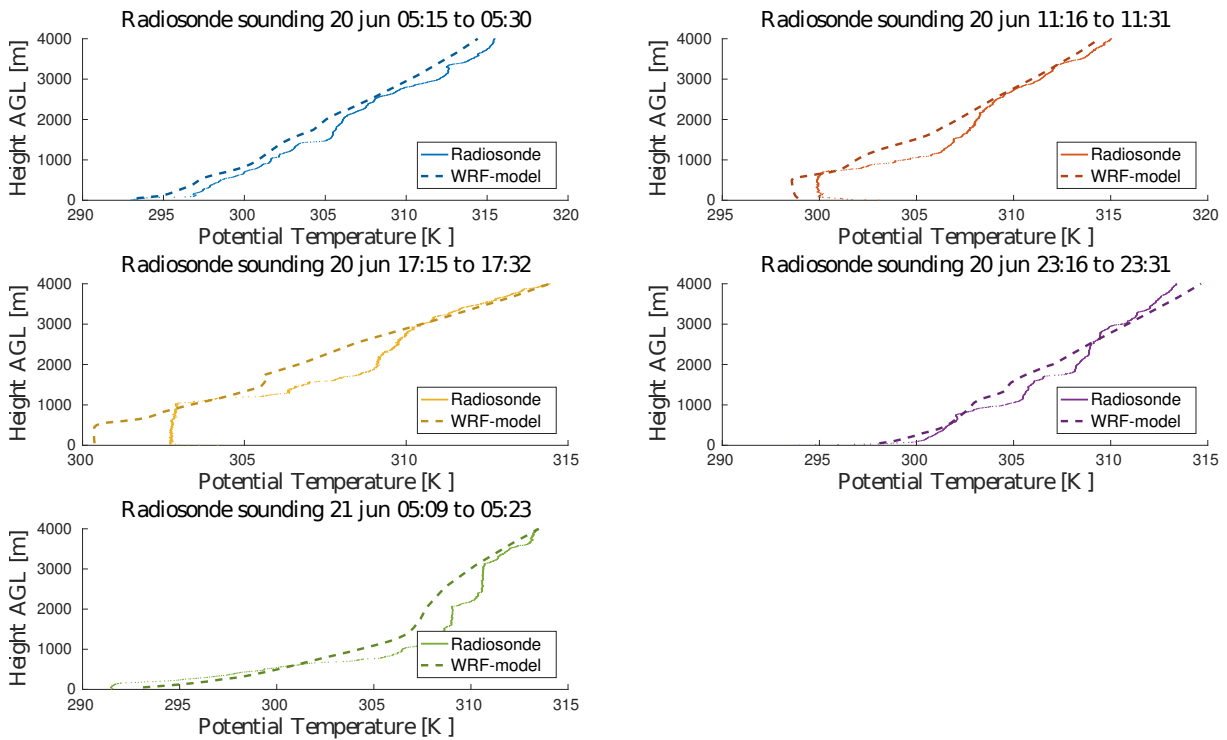
Figure 15. Vertical profiles of potential temperature for 5 different time periods (time in UTC). The solid line indicates observations from a radiosonde and the dashed line indicates values obtained from WRF.

Figure 16 and 17 display the vertical wind profiles and show that WRF is challenged at low altitudes. Wind direction at low altitude is a difficult quantity as shown in the observed variability consists of both real variability and measurement uncertainty. One should bear in mind that the lower atmosphere at *Plateau de Lannemezan* might experience local fluctuations which are unable to be resolved by a simulation with 3 km resolution no matter how effective the parameterization schemes are. The wind changes direction as the altitude increase. As the direction changes WRF outputs low windspeeds which are not necessarily present in the in situ observations.
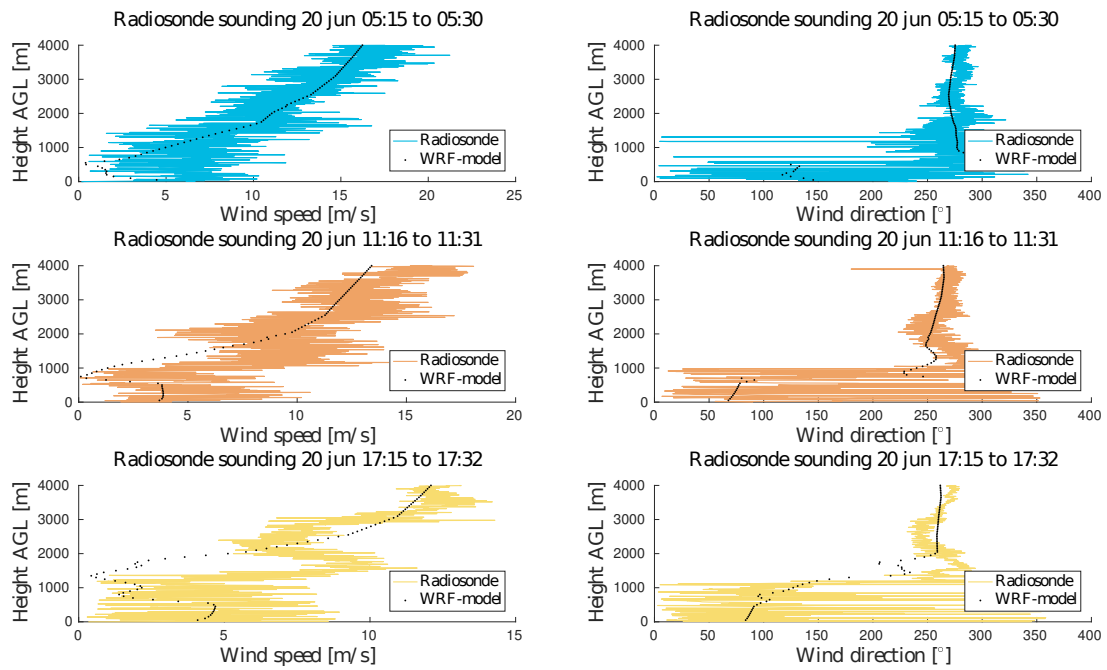
Figure 16. Vertical profiles of wind speed and wind direction observed by radiosondes as well as simulated by WRF (time in UTC). The lines show results made from radiosonde observations and the black dots show model results. Observations from three of the five radiosondes are seen in the figure.
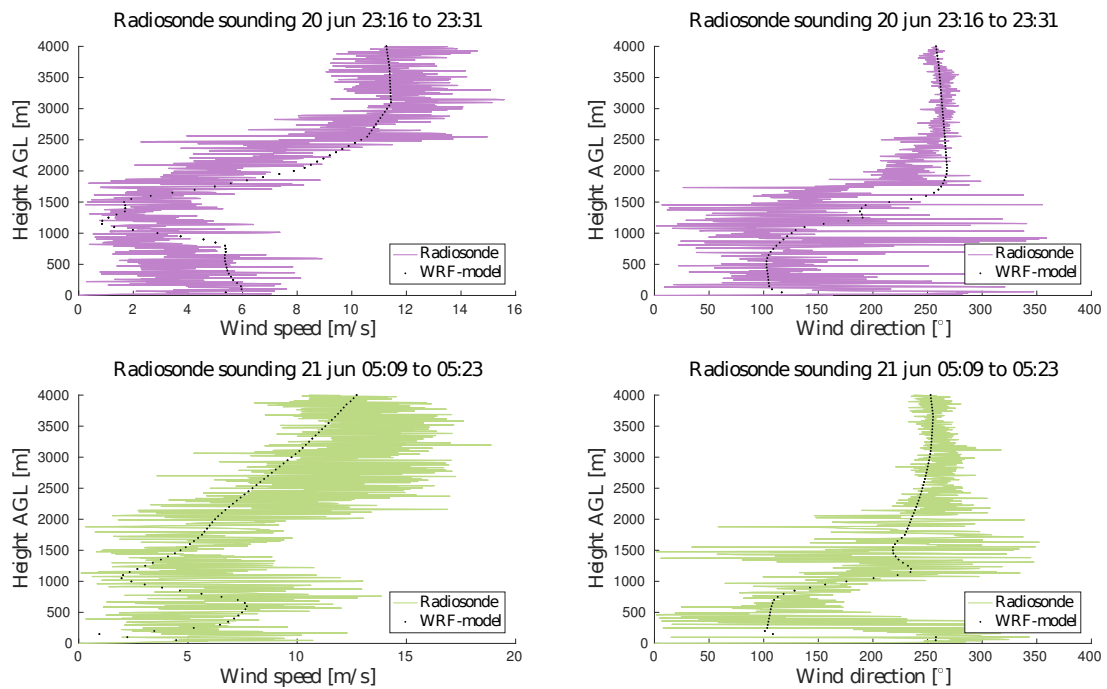
Figure 17. Vertical profiles of wind speed and wind direction observed by radiosondes as well as simulated by WRF (time in UTC). The lines show results made from radiosonde observations and the black dots show model results. Observations from three of the five radiosondes are seen in the figure.

4.2 FNL and ERA comparison

This section contain results used to make a comparison between the WRF input data. The comparison is based upon the mean value of variables in certain layers with respect to the planetary boundary layer height. The layers are divided into the *bottom half* of the planetary boundary layer, the *top half* of the planetary boundary layer and up to *500 m above* the planetary boundary layer. The boundary layer height used is an estimate from a UHF wind profiler using the air refractive index structure coefficient. An example of the layers and time periods is shown below for the reference simulation in figure 18.
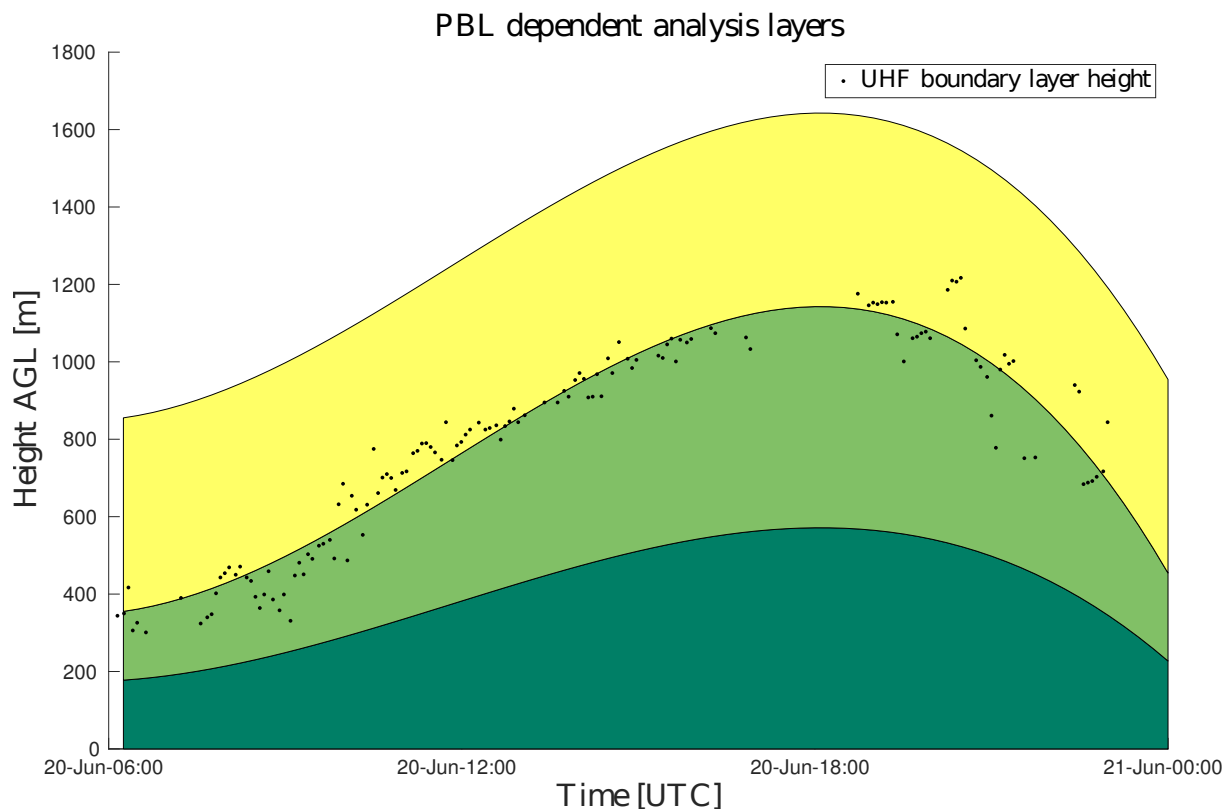
Figure 18. The comparison between simulated and observed wind-direction and wind-speeds are limited to 3 PBL dependent layers. The layers are ordered as *PBL bottom*, *PBL top* and *above PBL*. The black dots indicate the observed PBL height. These are the analysis layers for the reference simulation.

Table 3 contain differences between the WRF simulation which used ERA and FNL input data. The results are quite mixed with some layers being very similar in both simulations whereas other layers are very different. The layer above the planetary boundary layer during the period 06:00 UTC to 12:00 UTC (corresponding to the formation of the planetary boundary layer) is an example of layer with a mismatch in wind direction. The mean of the absolute errors indicate a directional difference of over 90 degrees. These winds are however quite weak indicating that this layer might be sensitive to perturbations caused by the input data.

Table 3. Mean horizontal wind speed v_H and mean meteorological wind direction ϕ for the three time periods and three different analysis layers with respect to the planetary boundary layer. The table contain data for making a comparison between model data which has used ERA input data and which has used FNL input data. The mean absolute error in the bottom rows quantify the difference between the two datasets.

Time [UTC]	06:00 - 12:00		12:00 - 18:00		18:00 - 00:00	
	v_H $[m/s]$	ϕ $[deg]$	v_H $[m/s]$	ϕ $[deg]$	v_H $[m/s]$	ϕ $[deg]$
ERA mean values						
PBL bottom	2.8038	88.374	4.3615	79.816	5.3251	103.17
PBL top	2.0155	89.564	2.3213	85.638	2.3213	85.638
Above PBL	1.5171	87.072	1.2502	145.63	1.2502	145.63
FNL mean values						
PBL bottom	2.7891	73.526	4.3549	75.517	6.5172	104.32
PBL top	2.429	97.581	2.5264	87.104	2.5264	87.104
Above PBL	0.91553	130.55	1.4995	140.51	1.4995	140.51
Mean absolute difference between ERA and FNL						
PBL bottom	0.1478	14.9194	0.0309	4.2997	1.1921	3.0341
PBL top	0.4152	8.8258	0.3337	9.9127	1.2421	4.0830
Above PBL	0.6016	109.8109	0.5340	17.8741	0.7676	9.9997

4.3 Planetary Boundary Layer Parameterization Scheme Comparison

Table 4 contain a comparison between the different planetary boundary layer parameterization schemes. The table contain mixed results. One could presume that there would be a relation between the schemes being local or non-local and TKE based and non-TKE based, however no clear distinction can be made. The MYJ- and YSU-scheme were generally in accordance with each other for different periods and PBL-areas. MYNN 2.5 predicted lower mean windspeeds than the other at the PBL bottom analysis layer. The 06:00 UTC to 12:00 UTC period above the boundary layer appear again as a difficult layer where YSU predicts a larger difference in mean wind direction.

Table 4. Mean horizontal wind speed v_H and mean meteorological wind direction ϕ for the three time periods and three different analysis layers with respect to the planetary boundary layer. The data is ordered after the three different planetary boundary layer scheme parameterizations tested.

Time [UTC]	06:00 - 12:00		12:00 - 18:00		18:00 - 00:00	
	v_H [m/s]	ϕ [deg]	v_H [m/s]	ϕ [deg]	v_H [m/s]	ϕ [deg]
MYJ mean values						
PBL bottom	2.8038	88.374	4.3615	79.816	5.3251	103.17
PBL top	2.0155	89.564	2.3213	85.638	2.3213	85.638
Above PBL	1.5171	87.072	1.2502	145.63	1.2502	145.63
MYNN 2.5 mean values						
PBL bottom	2.2412	84.361	3.2542	74.544	4.3073	101.36
PBL top	1.8609	90.432	2.7847	91.719	2.7847	91.719
Above PBL	1.4968	90.646	1.2915	154.35	1.2915	154.35
YSU mean values						
PBL bottom	2.7173	85.531	3.9423	72.105	5.3561	99.412
PBL top	1.9296	89.188	2.7944	94.265	2.7944	94.265
Above PBL	1.4373	109.41	1.3755	155.9	1.3755	155.9

4.4 Cumulus Parameterizaton Scheme Comparison

The differences in cumulus parameterization scheme are seen in table 5. There is litte difference in which cumulus parameterization scheme that was used. This is expected as only the coarse parent domain with 9 km horizontal resolution could be expected to have difficulties resolving cumulus convection and possibly benefit from any cumulus parameterization scheme. The parent domain provides boundary conditions to the inner domain and thus the cells at *Plateau de Lannemezan*. It is the effect from the differences in boundary conditions that are seen in the table.

Table 5. Mean horizontal wind speed v_H and mean meteorological wind direction ϕ for the three time periods and three different analysis layers with respect to the planetary boundary layer. The table contains data for the three different cumulus parameterization schemes tested.

Time [UTC]	06:00 - 12:00		12:00 - 18:00		18:00 - 00:00	
	v_H [m/s]	ϕ [deg]	v_H [m/s]	ϕ [deg]	v_H [m/s]	ϕ [deg]
KF mean values						
PBL bottom	2.8038	88.374	4.3615	79.816	5.3251	103.17
PBL top	2.0155	89.564	2.3213	85.638	2.3213	85.638
Above PBL	1.5171	87.072	1.2502	145.63	1.2502	145.63
BMJ mean values						
PBL bottom	2.8055	88.149	4.287	79.877	6.0844	106.71
PBL top	2.0222	89.338	2.2466	87.794	2.2466	87.794
Above PBL	1.5133	87.646	1.3324	136.26	1.3324	136.26
NO SCHEME mean values						
PBL bottom	2.8044	88.34	4.3265	78.973	5.7094	104.09
PBL top	2.0163	89.574	2.2271	84.416	2.2271	84.416
Above PBL	1.5165	87.189	1.2364	139.04	1.2364	139.04

4.5 Quantitative Comparison of Simulations

This section presents data which give an overview of the results relating to planetary boundary layer regions for all six simulations as well as the respective data collected from the two radiosondes. Table 6 below give an overview of all the different simulations that were done for a period with still increasing planetary boundary layer (the period starting at 11:16 UTC) and as it start to peak (the period starting at 17:16 UTC) as well as radiosonde observations. All simulations underestimate the mean potential temperature inside the planetary boundary layer by about 1 K. Near 11:16 UTC the mean wind speed is underestimated inside the planetary boundary layer by approximately 2 m/s and underestimated above the planetary boundary layer by approximately 5 m/s. The mean wind direction inside the planetary boundary layer at this time was off by varying amounts but all above 50 degrees (some nearing as much as 80 degrees). Near 17:16 UTC the mean winds are also underestimated by the WRF simulations with the biggest difference being the area above the planetary boundary layer (an error of approximately 2 m/s). At this time period the mean wind direction is moderately accurate but with the MYNN 2.5 and YSU planetary boundary layer schemes having inaccuracies above the planetary boundary layer.

The different schemes and choice of input data are generally consistent with one another. The simulation with the MYNN 2.5 planetary boundary scheme appear as an outlier in regard to the wind. This was previously discussed in the evaluation of the planetary boundary layer parameterization schemes.

Table 6. Mean potential temperature θ, mean horizontal wind speed v_H and mean meteorological wind direction ϕ for each WRF simulation for two short time periods and two layers with regard to the PBL . The *Radiosonde* entry denotes two of the radiosondes used to make in situ observations.

Time [UTC]	11:16 —			17:16 —		
	$\theta\,[k]$	$v_h\,[m/s]$	$\phi\,[deg]$	$\theta\,[k]$	$v_h\,[m/s]$	$\phi\,[deg]$
ERA-MYJ-KF mean values						
In PBL	299.08	3.063	87.338	300.46	4.4267	90.09
Above PBL	302.07	1.6553	242.5	302.77	1.8845	113.79
FNL-MYJ-KF mean values						
In PBL	298.43	3.5079	79.35	300.61	4.389	85.591
Above PBL	302.06	0.89709	171.6	303.09	2.2139	103.83
ERA-MYNN 2.5-KF mean values						
In PBL	298.88	2.8311	75.361	300.42	3.1923	89.698
Above PBL	301.69	1.2814	192.58	303.76	2.081	158.18
ERA-YSU-KF mean values						
In PBL	299.22	3.069	78.717	300.89	3.7993	88.593
Above PBL	301.92	1.7471	222.17	303.34	1.6743	161.32
ERA-MYJ-BMJ mean values						
In PBL	299.06	3.0746	86.75	300.52	3.8888	89.003
Above PBL	302.05	1.6462	242.01	302.98	1.2779	125.95
ERA-MYJ-NONE mean values						
In PBL	299.08	3.0653	87.394	300.46	4.5306	88.656
Above PBL	302.07	1.6563	242.38	302.84	1.7862	110.8
RADIOSONDES mean values						
In PBL	300.13	5.3513	143.61	302.75	4.8095	99.856
Above PBL	304.52	6.5134	245.07	302.98	4.1833	113.97

4.6 Wind Profiler Observations

Table 7 provide mean values for horizontal wind speed v_h and meteorological wind direction ϕ in the previously defined layers and time periods as collected from a UHF wind profiler. These values can be compared to table 3, table 4 and table 5 to evaluate the individual simulations against real observations. Doing this the layer above the planetary boundary layer for example appear as a problem for each simulation as the wind speed is consistently underestimated and as there are errors in the wind direction.

Table 7. Observed mean values from a UHF wind profiler. Mean horizontal wind speed v_H and mean meteorological wind direction ϕ for each WRF simulation for the three time periods and three layers with regard to the PBL.

Time [UTC]	06:00 - 12:00		12:00 - 18:00		18:00 - 00:00	
	$v_H\ [m/s]$	$\phi\ [deg]$	$v_H\ [m/s]$	$\phi\ [deg]$	$v_H\ [m/s]$	$\phi\ [deg]$
UHF WIND PROFILER mean values						
PBL bottom	2.6688	66.796	4.5562	53.648	4.6321	95.87
PBL top	2.3241	97.982	3.7031	90.078	3.7031	90.078
Above PBL	3.3677	116.63	6.0548	88.808	6.0548	88.808

5 Discussion

It has been shown that WRF had difficulties in modelling a layer above the planetary boundary layer top. This problematic layer is most consistent when using the boundary layer height as estimated from the air refractive index structure coefficient, but is also valid until about 15:00 UTC when using the estimate based on the TKE dissipation rate. These different estimates are discussed further in e.g. Nilsson et al. (2015) and Couvreux et al. (2016). As the air refractive index structure coefficient is most efficient in defining the problematic layer it could serve as helpful information in troubleshooting the underlying cause. Assumpions should however be made with caution as the boundary layer height estimates during the evening might reflect some other process than a boundary layer related one. These results do however indicate an importance in the estimation of the planetary boundary layer height when evaluating variables at altitudes near the planetary boundary layer height, at least during the non-dissipative period.

Angevine et al. (2014) show that initializing the soil variables with ERA in the study region result in a cool and wet soil bias which negatively affected the planetary boundary layer and might help to explain some of the planetary boundary layer related errors and how these might be remedied.

The variability in the wind profiles from the radiosondes can be supplemented by profiles from both available UHF wind profilers, sodar instrumentation, radiosondes and the 60 m tower. These additional observations could be used in future work to better characterise this indicated variability in the mixed layer. The WRF reference run

used a total of 50 vertical levels and is unable to express such an inconsistent wind field as found from the real observations where fluctuations are present in turbulence.

A figure of the horizontal wind profiles are presented in Appendix C in figure 19 for ERA and FNL to provide a graphical comparison. Unrelated to any boundary layer transition it is interesting to note a pronounced sensitivity to input data in the stable and well-mixed lower atmosphere which occur during the evening and night. The FNL input data leads to much stronger winds than the ERA input data (as seen in figure 19).

As there is little difference between the two cumulus parameterization schemes (KF and BMJ) and the use of no scheme at all it is possible that even the 9 km coarse parent domain can adequately resolve cumulus convection and other phenomena and quantities associated with the cumulus parameterization scheme during this period. The studied period had relatively low amounts of clouds which mean that the cumulus parameterization scheme had less importance. By studying periods with more clouds the differences from the choices of cumulus parameterization scheme is expected to become more apparent.

6 Conclusions

The study area located on a plateau north of the Pyrenees subject to both mountain-wind system effects and planetary boundary layer effects had an apt but improvable representation when simulated with WRF 3.7.1 with the reference set-up parameters. Effects from both the planetary boundary layer and the mountain-wind system could be seen in the results. The conclusion is based upon evaluation of the WRF results when compared with in situ observations of potential temperature, wind velocity and wind direction collected from radiosondes and a wind profiler. The largest errors were found in conjunction with the boundary layer depth as estimated by *air refractive index structure coefficient* from a wind profiler which implicate an importance in describing planetary boundary layer effects in the model. These errors may be remedied by applying a surface spinup method as described in Angevine et al. (2014).

The six different simulations that were performed had similar results with a few but generally uncommon outliers in the evaluation. There were differences in the wind fields when using ECMWF ERA input data and FNL input data. The mean absolute error in the wind speed between the two were approximately 1.2 m/s. The difference in wind direction was larger (mean absolute error of up to about 110 degrees) but this error is amplified by the layer having low wind speeds and is not as dramatic as it seems.

Each tested planetary boundary layer parameterization scheme had its own characteristics. The MYNN 2.5 planetary boundary layer scheme resulted in lower wind-speeds. During the period in which the boundary layer forms each scheme predicted different wind directions for a layer 500 m above the planetary boundary layer height as obtained from wind profiler measurments. This consistently appear as a problematic layer with a sensitivity to perturbations.

The choice of cumulus convection parameterization schemes had little to no importance when simulating the coarse parent domain as shown by the results. The coarse

domain with 9 km horizontal resolution might be able to adequately resolve necessary cumulus convection events to provide accurate boundary conditions to the subdomain. Simulating additional days with more pronounced cloud cover may better reveal the differences that the choice give rise to.

Simulating locations within complex wind systems is possible with WRF. The choice of input data and planetary boundary layer schemes are details worthy of scrutiny as ECMWF ERA input data had better performance than NCEP FNL input data, as well that the MYJ planetary boundary layer had the best performance in comparison to radiosondes.

References

Ahrens, C. D. & Perry J. S. (2009). *Extreme weather and climate*. Belmont, CA: Brooks-Cole, Cengage Learning.

Angevine, W. M., Bazile, E., Legain, D. & Pino, D. (2014). Land surface spinup for episodic modeling. *Atmospheric Chemistry and Physic*, vol. 14(15), pp. 8165–8172.

Collins, S. N., James, R. S., Ray, P., Chen, K., Lassman, A. & Brownlee, J. (2013). Grids in Numerical Weather and Climate Models. In: Zhang, Y. & Ray, P. (ed), *Climate Change and Regional/Local Responses*. (n.p.): InTech. pp. 111-128. DOI: 10.5772/55922.

Couvreux, F., Bazile, E., Canut, G., Seity, Y., Lothon, M., Lohou, F., Guichard, F. & Nilsson, E. (2016). Boundary-layer turbulent processes and mesoscale variability represented by Numerical Weather Prediction models during the BLLAST campaign. *Atmos. Chem. Phys. Discuss.*, vol. 16, pp. 1–35. DOI:10.5194/acp-2015-1042.

Hu, X.-M., Nielsen-Gammon, J. W. & Zhang, F. (2010). Evaluation of Three Planetary Boundary Layer Schemes in the WRF Model. *Journal Of Applied Meteorology and Climatology*, vol. 49, pp. 1831-1844. DOI: 10.1175/2010JAMC2432.1.

Nilsson, E., Lothon, M., Lohou, F., Pardyjak, E., Hartogensis, O. & Darbieu, C. (2015). Turbulence Kinetic Energy budget during the afternoon transition - Part 2: A simple TKE model. *Atmos. Chem. Phys. Discuss.*, vol. 15, pp. 29807–29869. DOI: 10.5194/acpd-15-29807-2015.

Quéno, L., Vionnet, V., Dombrowski-Etchevers, I., Lafaysse, M., Dumont, M. & Karbou, F. (2016). Snowpack modelling in the Pyrenees driven by kilometric resolution meteorological forecasts. *The Cryosphere Discussions*, vol. 16, pp. 1–32. DOI: 10.5194/tc-2016-20.

Reynolds, K. (1995). Pyrenees 3000. *The Alpine Journal*, vol. 100. URL: http://www.alpinejournal.org.uk/Contents/Contents_1995.html.

Skamarock, W. C., Klemp, J. B., Dudhia, J., Gill, D. O., Barker, D. M., Duda, M. G., Huang, X.-Y., Wang, W. & Powers, J. G. (2008). *A Description of the Advanced Research WRF Version 3*. NCAR/TN-475+STR. NCAR Technical Note. DOI: 10.5065/D68S4MVH.

Stensrud, D. J. (2007). *Parameterization schemes*. Cambridge: Cambridge University Press. DOI: 10.5772/55922.

Zardi, D. & Whiteman, C. D. (2013). Diurnal Mountain Wind Systems. In: Chow, K. F., De Wekker, F. J. S. & Snyder, J. B. (ed), *Mountain Weather Research and Forecasting: Recent Progress and Current Challenges*. Dordrecht: Springer Netherlands. pp. 35–119. DOI: 10.1007/978-94-007-4098-3_2.

Internet Sources

BLLAST (2011a). *2011 Field campaign Experimental Plans*. http://bllast.sedoo.fr/campaigns/ 2011/ [05/20/2016].

— (2011b). *Area and Time Frame*. http://bllast.sedoo.fr/campaigns/2011/introduction/area_time_frame.php [05/13/2016].

— (2015). *Arpege*. http://boc.sedoo.fr/nwp/lammodel/arpege/index.en.php?current=20110620 [05/13/2016].

ECMWF (2016). *ERA-Interim*.
http://www.ecmwf.int/en/research/climate-reanalysis/era-interim [05/12/2016].

The COMET Program (2009). *Impact of Model Structure and Dynamics - version 2*.
http://www.meted.ucar.edu/nwp/model_structure/print.htm [05/13/2016].

UCAR (2016a). *NCEP FNL Operational Model Global Tropospheric Analyses, continuing from July 1999*. http://rda.ucar.edu/datasets/ds083.2/ [05/12/2016].

— (2016b). *Overview of NCL*. http://www.ncl.ucar.edu/overview.shtml [05/13/2016].

Whiteman, C. D. (2014). *Diurnal wind system variation in the appalachian mountain range*.
https://commons.wikimedia.org/wiki/File:Diurnal_mountain_winds_variation.jpg [05/10/2016].

Appendices

Appendix A.   WRF in Practice

In this appendix I provide some background on working with WRF and some of my experience in learning- and modelling with it. Modelling with WRF has been a cornerstone of my project and my recount might serve as an interesting insight to the reader. What is required to use WRF and what does it practically amount to?

WRF is an open source project and the software is provided by UCAR as source code. This means that the user themselves need to compile the software. Both the model portion (denoted just by WRF) and the preprocessing system WPS need to be individually compiled. This can be done on both *Windows* and *Linux* platforms. The Windows platform however need additional steps to setup an *Unix* environment which WRF requires (something which is already integrated and a core part of GNU/Linux). Any Linux distribution has the potential to run WRF. I decided to use Linux. I had the best experience with a *Debian* based distributions (such as *Ubuntu* or *Mint*) as I ran into unresolved problems using my first choice *Arch Linux* which were not present with a Debian based distribution (I ran into open source Fortran compiler error messages when compiling WRF). Someone more versed in using Linux might find a resolution to these problems or they might not persist as WRF or other software are provided updates.

The WRF and WPS source code come with sophisticated build mechanisms which facilitates the compilation. What is needed by WRF is precompiled libraries with a setup Unix environment with the libraries and compiler options assigned to variables and library paths defined. The only required library is *netCDF* which provide the gridded I/O filesystem WRF uses. I compiled additonal libraries to provide support for the *GRIB2* filesystem in addition to native *GRIB1* which might be useful when preproccessing input data to WPS. The libraries need be compiled with the same compiler that will be used for WRF, and afterwards WPS. All this information is incredibly well documented on the UCAR WRF website and in the WRF documents.

With these sometimes complicated steps completed terrestrial data need to be supplied for WPS such that it later can be interpolated together with meteorological data to complete WRF input files. This data is provided by UCAR and can be downloaded for use with WRF with different resolutions and number of variables. Using the UCAR provided terrestrial data is simple as it already has correct format to be used by WPS. The meteorological data required to do non-ideal simulations need to be acquired and setup with WPS. As each source of gridded meteorological data potentially have different formats an explicit specification of the data format is required. Thankfully WRF is provided with a set of such specifications (called *Vtables*, presumably from Variable tables). The process of specifying to WPS which format the gridded meteorological data has is done by using a helpful shell script provided with the source code.

After these steps the time has come to setup the WRF domains. This involves editing a text file called a namelist and changing values and fields as necessary for the

customization of the simulation. This for example involves adding columns for nested domains. Editing the namelist is a pretty intuitive process as the variables have descriptive names. Setting up the nested domains is however not so intuitive as one needs to have a grasp on the internal WRF coordinate system which is used to describe where inside a parent domain a nested domain has its corners. This is not at all challenging but the arithmetic required might come as a surprise. An alternative is to compile a tool which can help in the domain setup, such as WRF *domain wizard* providing a graphical user interface for some steps, but learning to use such a program also come with some learning curve.

With a setup domain, terrestrial data and specified gridded meteorological data WPS is then used to interpolate this data onto the specified domain, outputting gridded files that WRF later can use as input to run the simulation. Using WPS consist of running three core programs which are supplied with the WPS compilation, which is *ungrib*, *geogrid* and *metgrid*. Ungrib creates intermediary files from the meteorological data and geogrid creates intermediary files from the terrestrial (geographic) data. These intermediary files are then passed to metgrid which performs the penultimate step of the preprocessing. The ultimate step is using a program external WPS and part of the WRF compilation called *real* (for real datacases, there exists other alternatives but they are for ideal simulations). After this WRF is supplied with its necessary simulation input data.

WRF like WPS has a configuration file which need to be edited per user requirements, another namelist which is more detailed as it also contains options and parameters for the actual simulation and not just the domains. This includes for example the simulation timestep or which physics schemes to use and for which domain. Appendix B contain such a namelist.

Above are the necessary steps required to reach the point where an actual simulation can be commenced. The simulation is commenced by calling the program called *wrf* from the terminal. I simulated 30 hour periods with 30 s timesteps for a 100 x 100 grid 9 x 9 km coarse domain with 50 vertical levels and with a nested subdomain with 3 x 3 km resolution. I had a different timestep at first which I had to adjust as WRF became unstable after a few hours (resulting in a crash) but the 30 s timestep worked without problems.

I performed my simulations on my personal computer which had a 1.7 GHz Intel i5 dual core processor. Using a single computer is a suboptimal choice. Each of the simulations took approximately 14 hours with this set up. About 100 hours of processing time have been required to complete the computer simulations during the span of this project. This was however just a minor inconvenience and to little consequence, but with faster simulation times doing spin-up simulations would have been a possibility if I would have decided to involve myself in that process. With my simulation times that is however an impossibility as it requires longer simulation periods which also effectively are simulated several times. Normally atmospheric simulations are done with computer clusters but this goes to show that it is not always necessary and can be done with a simple everyday laptop.

Appendix B.   Reference Run Configuration

`namelist.input` contents:

```
&time_control
run_days                 = 01,
run_hours                = 06,
run_minutes              = 0,
run_seconds              = 0,
start_year               = 2011,     2011,
start_month              = 06,       06,
start_day                = 20,       20,
start_hour               = 00,       00,
start_minute             = 00,       00,
start_second             = 00,       00,
end_year                 = 2011,     2011,
end_month                = 06,       06,
end_day                  = 21,       21,
end_hour                 = 06,       06,
end_minute               = 00,       00,
end_second               = 00,       00,
interval_seconds         = 21600,
input_from_file          = .true.,   .true.,
history_interval         = 15,       15,
frames_per_outfile       = 8,        8,
restart                  = .false.,
restart_interval         = 5000,
io_form_history          = 2,
io_form_restart          = 2,
io_form_input            = 2,
io_form_boundary         = 2,
debug_level              = 0,
/

&domains
time_step                = 30,
time_step_fract_num      = 0,
time_step_fract_den      = 1,
max_dom                  = 2,
e_we                     = 100,      136,
e_sn                     = 100,       88,
e_vert                   = 50,       50,
p_top_requested          = 5000.0,
num_metgrid_levels       = 27,
num_metgrid_soil_levels  = 4,
dx                       = 9000,     3000,
dy                       = 9000,     3000,
grid_id                  = 1,        2,
parent_id                = 1,        1,
i_parent_start           = 1,        29,
j_parent_start           = 1,        31,
parent_grid_ratio        = 1,        3,
parent_time_step_ratio   = 1,        3,
feedback                 = 1,
smooth_option            = 0,
eta_levels               = 1.000, 0.999, 0.998, 0.997, 0.996,
                 0.995, 0.994, 0.993, 0.992, 0.991,
                 0.99, 0.988, 0.986, 0.984, 0.982,
                 0.98, 0.978, 0.976, 0.974, 0.972,
                 0.97, 0.96, 0.95, 0.94, 0.93,
                 0.92, 0.91, 0.9, 0.89, 0.88,
                 0.87, 0.86, 0.85, 0.84, 0.83,
                 0.82, 0.81, 0.8, 0.75, 0.7,
                 0.65, 0.6, 0.55, 0.5, 0.45,
```

```
                         0.4,  0.3,  0.2,  0.1,  0.000,
 /


 &physics
 mp_physics               = 3,          3,
 ra_lw_physics            = 4,          4,
 ra_sw_physics            = 4,          4,
 radt                     = 3,          3,
 sf_sfclay_physics        = 2,          2,
 sf_surface_physics       = 2,          2,
 bl_pbl_physics           = 2,          2,
 bldt                     = 0,          0,
 cu_physics               = 1,          0,
 cudt                     = 0,          0,
 isfflx                   = 1,
 ifsnow                   = 0,
 icloud                   = 1,
 surface_input_source     = 1,
 num_soil_layers          = 4,
 sf_urban_physics         = 0,          0,
 maxiens                  = 1,
 maxens                   = 3,
 maxens2                  = 3,
 maxens3                  = 16,
 ensdim                   = 144,
 sst_update               = 0,
 /

 &fdda
 /


 &dynamics
 w_damping                = 1,
 diff_opt                 = 1,
 km_opt                   = 4,
 diff_6th_opt             = 2,          2,
 diff_6th_factor          = 0.12,       0.12,
 base_temp                = 290.,
 damp_opt                 = 0,
 zdamp                    = 5000.,      5000.,
 dampcoef                 = 0.01,       0.01,
 khdif                    = 0,          0,
 kvdif                    = 0,          0,
 non_hydrostatic          = .true.,     .true.,
 moist_adv_opt            = 2,          2,
 scalar_adv_opt           = 2,          2,
 /


 &bdy_control
 spec_bdy_width           = 5,
 spec_zone                = 1,
 relax_zone               = 4,
 specified                = .true.,    .false.,
 nested                   = .false.,    .true.,
 /


 &grib2
 /


 &namelist_quilt
 nio_tasks_per_group      = 0,
 nio_groups               = 1,
 /
```

Appendix C.   Supplemental Figures: ERA - FNL comparison

Figure 19. Interpolated horizontal wind fields for ERA (top) and FNL (bottom) input data.